Journal of Materials Chemistry C

ROYAL SOCIETY OF CHEMISTRY

PAPER

View Article Online
View Journal

Cite this: DOI: 10.1039/d6tc00535g

Reorientational dynamics of methylbenzylammonium cations in the chiral metal halide composite MBAMnCl$_3$·2H$_2$O

Kanming Shi,[a] Weidong Cai,[b] Jiajun Qin,[b] Lars Öhrström,[a] Fanni Juranyi,[c] Feng Gao[b] and Maths Karlsson*[a]

We report results from quasielastic neutron scattering (QENS) measurements of the organic cation dynamics in the manganese-based organic–inorganic chiral metal halide composites (*R*)-MBAMnCl$_3$·2H$_2$O and (*S*)-MBAMnCl$_3$·2H$_2$O, where (*R*)-/(*S*)-MBA (methylbenzylammonium) = $C_6H_5CH(CH_3)NH_3^+$. Measurements upon heating from 44 to 375 K reveal how the dynamics evolve from (an)harmonic vibrations to localized, reorientational motions of the (*R*)-/(*S*)-MBA cations at approximately 270 K, for both materials. Analysis of the elastic incoherent structure factors (EISFs) of the materials suggests that the spatial geometry of the reorientational dynamics changes, and becomes more complex, with increasing temperature. Up to 325 K, the dynamics can be described as three-fold (C_3) jump-diffusion dynamics or continuous rotational diffusion of the methyl ($-CH_3$) and ammonium ($-NH_3$) groups of the (*R*)-/(*S*)-MBA cations. At higher temperatures, 350–375 K, the analysis points towards the additional presence of continuous rotational diffusion of the $-C_6H_5$ group of the (*R*)-/(*S*)-MBA cation around its long molecular axis, as well as a whole-cation reorientation, here described as two-fold (C_2) jump-diffusion dynamics between two different cation orientations. Such whole-cation dynamics have previously been observed mainly in materials with smaller organic cations. This suggests that the dynamics of the (*R*)-/(*S*)-MBA cation are relatively mobile in nature, with relatively weak interactions with the surrounding lattice.

Received 18th February 2026,
Accepted 28th May 2026

DOI: 10.1039/d6tc00535g

rsc.li/materials-c

1 Introduction

Metal halide perovskites (MHPs), of the general three-dimensional (3D) ABX_3 structure, and their low-dimensional variants, such as two-dimensional (2D) A_2BX_4, where A is an organic cation, B is a metal cation, and X is a halide anion, are valued for their unique optoelectronic properties and promise for application in both solar cells[1,2] and light emitting diodes.[3,4] Furthermore, they show promise for application in low-dimensional magnetism[5] and thermoelectrics.[6] However, a critical challenge in this field is to understand how the optoelectronic properties are related to the dynamical properties of the materials, especially with regard to the organic cation dynamics.

The current understanding of the organic cation dynamics in MHPs is based primarily on results obtained from computer simulations, nuclear magnetic resonance and QENS experiments. QENS studies, which are of specific concern here, have mostly focused on the prototypical 3D MHPs (MA,FA)PbX$_3$ (MA = methylammonium; FA = formamidinium; X = I, Br).[7–15] For low-dimensional MHPs, QENS studies of the organic cation dynamics have focused on the 2D MHPs BA_2PbBr_4 (BA = butylammonium), $ODAPbBr_4$ and $GABA_2PbBr_4$ (ODA = 1,8-diaminooctammonium, and GABA = 4-aminobutyric acid),[16] BA_2PbI_4 and PEA_2PbI_4 (PEA = phenetylammonium),[17,18] $(OA)_2PbI_4$ (OA = octylammonium),[19] and, most recently, (1,3-PDA)PbBr$_4$ (PDA = phenylenediammonium), (1,4-PDA)PbBr$_4$, and (1,4-XDA)PbBr$_4$ (XDA = xylylenediammonium), and the zero-dimensional (0D) "perovskitoid" (1,3-XDA)$_2$PbBr$_6$.[20] QENS studies have, typically, revealed various rotational (reorientational) motions of the organic cations, on the 1–100 ps timescale, and how the timescale and geometry of the dynamics change with temperature, which in some cases have been correlated with the materials' optoelectronic properties.[16,17,20]

Here, in a variable temperature QENS study, we investigate the nature of organic cation dynamics in the novel, manganese (Mn)-based chiral MHPs (*R*)-/(*S*)-MBAMnCl$_3$·2H$_2$O, also formulated as (*R*)-/(*S*)-(HMBA)$_2$[Mn$_2$Cl$_6$(H$_2$O)$_4$].[21–23] These materials show promise for use in applications such as circular dichroism

[a] Department of Chemistry and Chemical Engineering, Chalmers University of Technology, SE-412 96, Göteborg, Sweden. E-mail: maths.karlsson@chalmers.se
[b] Department of Physics, Chemistry and Biology (IFM), Linköping University, SE-581 83, Linköping, Sweden
[c] PSI Center for Neutron and Muon Sciences, 5232, Villigen PSI, Switzerland

and circularly polarized light,[24] with potential application in, *e.g.*, quantum computing,[25] data storage and encryption,[26] biomolecular sensing,[27] imaging,[28] and asymmetric photochemical synthesis,[29] which may not be achievable with achiral MHPs. Compared to the prototypical chiral MHP (*R*)-/(*S*)-MBA_2PbI_4,[30] (*R*)-/(*S*)-$MBAMnCl_3{\cdot}2H_2O$ is a lead-free and hence more environmentally benign material. Additionally, the presence of luminescent Mn^{2+} ions gives rise to luminescence in the green and red wavelength regions, based on electronic d–d transitions,[30] which, along with blue emission originating from the (*R*)-/(*S*)-MBA cations, results in a broadband emission.[22] The aim of the study is to determine the nature of the organic cation dynamics, how it evolves with temperature and relates to the nature of organic cation dynamics in other MHPs, and how it correlates with the luminescence properties of the materials.

2 Experimental details

2.1 Sample synthesis and structural analysis

Powder samples of (*R*)-/(*S*)-$MBAMnCl_3{\cdot}2H_2O$, approximately 0.3 g per composition, were prepared by grinding single crystals of the respective material. Single crystals of (*R*)-/(*S*)-$MBAMnCl_3{\cdot}2H_2O$ were prepared by first dissolving (*R*)-/(*S*)-MBA (1 mmol), manganese(II) chloride (1 mmol), and hydrochloric acid (1 mmol) in ethanol (30 mL), which was immediately followed by slow evaporation of ethanol at room temperature for about one week. When the synthesis occurs in a relatively humid environment, crystallization by evaporation at room temperature becomes difficult. It is necessary to heat the mixed solution to 40–60 °C to facilitate crystallization. Finally, the material is dried and then annealed in a furnace at about 60 °C for one hour. The yield of all Mn-based organic–inorganic halide materials is about 60–70%. All chemicals (α-methylbenzylamine (99%), hydrochloric acid (48 wt% in H_2O, ≥99.99%), manganese(II) chloride ($MnCl_2$, 99.9%), and ethanol (C_2H_5OH, 99.7%)) were commercially purchased from Sigma-Aldrich and used without further purification.[22]

Measurements and analyses of single-crystal and powder X-ray diffraction (SCXRD and PXRD) data of the samples (SCXRD used the (*R*)-$MBAMnCl_3{\cdot}2H_2O$ sample) confirmed phase purity and that the structures of both materials are in agreement with the structures reported in ref. 21, see S1 in the supporting information (SI). Specifically, (*S*)-$MBAMnCl_3{\cdot}2H_2O$ exhibits an orthorhombic structure of space group $P2_1$, with the lattice parameters a = 6.0631(2) Å, b = 36.3750(10) Å, and c = 6.3840(2) Å.[23] It may be described as a 0D MHP with two edge-shared $[MnCl_6]$ octahedra but with two of the Cl atoms replaced by H_2O molecules. These $[Mn_2Cl_8(H_2O)_4]^{2-}$ dimers are surrounded by (*S*)-MBA cations with strong interactions between the hydrogens of the (*S*)-MBA cations and the Cl atoms (Fig. 1).

2.2 Quasielastic neutron scattering

The QENS experiment was performed on the direct geometry time-of-flight spectrometer FOCUS at the Swiss Spallation Neutron Source SINQ at the Paul Scherrer Institute in Switzerland.[31,32]

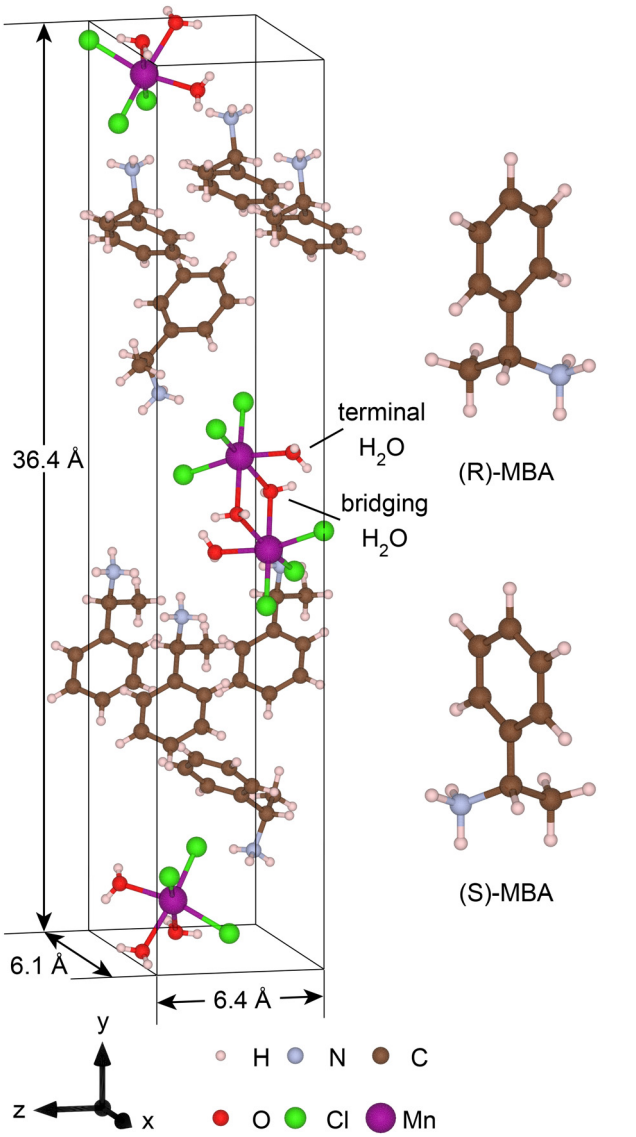

Fig. 1 Schematic illustration of (left) the crystal structure of (*S*)-$MBAMnCl_3{\cdot}2H_2O$ and (right) the (*R*)-MBA and (*S*)-MBA cations.[23] The solid lines represent the unit cell.

Each sample was finely distributed in an aluminium foil rolled cylinder whose expanded size was 5 cm × 4 cm. The aluminium foil was put in an aluminium can, which was sealed with a lead wire. We first took short (5 min) measurements upon cooling from 340 to 44 K (cooling rate ≈2.5–3.5 K min^{-1}), using 4 Å incident wavelength neutrons. The usage of 4 Å incident wavelength neutrons yielded an energy resolution at the elastic line of around 0.2 meV at full width at half maximum (FWHM, Γ), an accessible energy transfer (E) range from −20 to 5 meV, and an accessible momentum transfer (Q) range from 0.53 to 2.63 $Å^{-1}$ around the elastic peak. This was immediately followed by long (2 h) measurements at T = 44, 270, 300, 325, 350, and 375 K. After general and instrument-specific data reductions and corrections of the data, that included normalization of the detector efficiency and subtraction of the scattering of the sample cell alone, the measured data were transformed into the dynamical

structure factor $S(Q,E)$, which results from the sum of coherent and incoherent scattering contributions. The $S(Q,E)$s, as presented here, were binned into 15 Q-values.

For (R)-/(S)-MBAMnCl$_3$·2H$_2$O, it is important to note that H contributes approximately 92% to the total scattering cross section of the investigated materials and that the scattering from H is predominantly incoherent. Since we do not expect any dynamics of the inorganic sub-lattice within the here probed timescale of picoseconds, the quasielastic scattering is assumed to be related to self-dynamics of the H of the organic cations; however, one should note that a smaller concentration of H is also present as bridging and terminal water molecules of the Mn–Cl complexes (see Fig. 1), which may contribute to quasielastic scattering. However, previous studies show that the H of the bridging and terminal water molecules experience stronger interactions with the neighboring Cl atoms,[33] suggesting that their reorientational dynamics, if they exist, occur on a slower timescale than the timescale of reorientational dynamics of (R)-/(S)-MBA. Therefore, any reorientational dynamics of these water molecules have not been considered here. All data manipulations were done using the software DAVE.[34]

3 Results and discussion

3.1 Elastic intensity scans and intensity maps

In order to determine the temperature range in which the organic cation dynamics is accessible to the instrument, we first analyze the temperature dependence of the elastic intensity (I_{elastic}), as here extracted by integration over the energy range of $-0.1 < E < 0.1$ meV. Fig. 2 shows the elastic intensity, as derived in this way, for both materials. The measurements upon cooling, which were performed first, show a marked increase in elastic intensity between 330 and 300 K, especially for (S)-MBAMnCl$_3$·2H$_2$O. Upon further cooling, the increase in elastic intensity occurs at a decreased and similar rate for both materials. The measurements upon heating follow the same trend as the measurements upon cooling, but show that the marked variation in elastic intensity (at 330–300 K) is shifted to higher temperatures by approximately 20 K. The marked change in elastic intensity in the temperature range of 300–350 K indicates the onset (on heating) and freezing out (on cooling) of diffusional dynamics in both materials, whereas the practically linear behavior below ≈300 K reflects the increase (upon temperature increase) and decrease (upon temperature decrease) of (an)harmonic vibrational dynamics in the materials. Due to the generally soft nature of MHPs, it is important to note that the material may exhibit pronounced anharmonicity even at temperatures well below the onset of reorientational dynamics.[35–37]

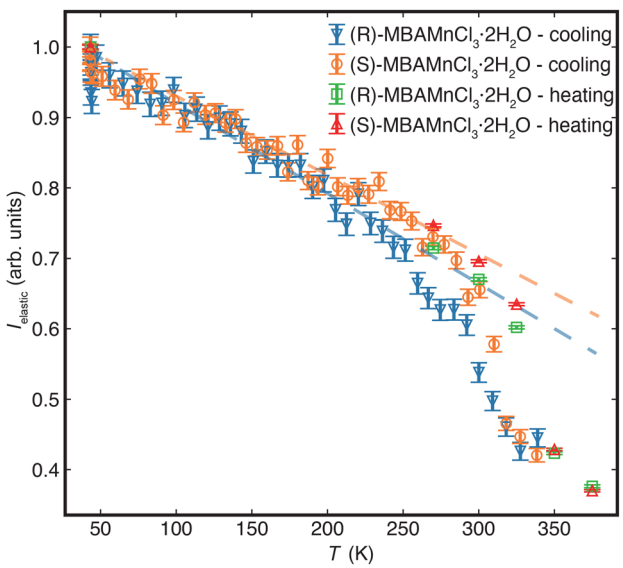

Fig. 2 Elastic intensity, I_{elastic}, of (R)-/(S)-MBAMnCl$_3$·2H$_2$O, as measured upon cooling (first cycle) and heating (second cycle). The data have been normalized to one at 44 K. The dashed lines are guides to the eye and manifest the practically linear behavior of the temperature dependence of the data below 200 K.

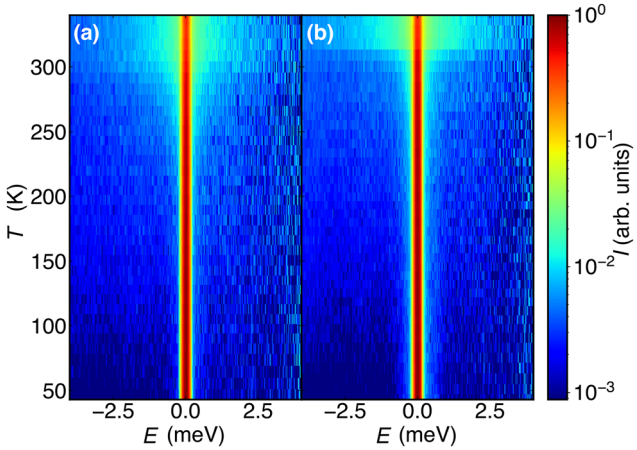

Fig. 3 $I(T,E)$ maps, as measured upon cooling for (a) (R)-MBAMnCl$_3$·2H$_2$O and (b) (S)-MBAMnCl$_3$·2H$_2$O. The data have been summed over the whole Q-range, 0.53–2.63 Å^{-1}.

The onset of diffusional dynamics of the MBA cations is further reflected in maps of the intensity of the scattered neutrons, as plotted as a function of temperature and energy transfer, [$I(T,E)$, see Fig. 3]. As can be seen, there is a clear quasielastic broadening at temperatures above approximately 250 K for (R)-MBAMnCl$_3$·2H$_2$O and 290 K for (S)-MBAMnCl$_3$·2H$_2$O, in quite good agreement with Fig. 2. We also observe that the quasielastic signal appears somewhat broader for (S)-MBAMnCl$_3$·2H$_2$O, as compared to (R)-MBAMnCl$_3$·2H$_2$O, thus indicating faster dynamics in the former.

3.2 Dynamical structure factors

For a detailed analysis of the neutron scattering data, $S(Q,E)$ was fitted to the following function:

$$S(Q,E) = \left[A_0(Q)\delta(E) + \sum_i^n A_i(Q)\mathscr{L}(E;\Gamma_i) + \mathrm{bkg}(Q)\right] \otimes [R(Q,E)\cdot I(Q)] \quad (1)$$

Here, $\mathscr{L}(E;\ \Gamma_i)$ are Lorentzian functions with FWHM Γ_i, bkg(Q) is a linear background, $A_0(Q)$ and $A_i(Q)$ are the elastic and quasielastic incoherent structure factors, which were normalized to $A_0(Q) + \sum A_i(Q) = 1$, and $R(Q,E)$ is the instrumental resolution function that is approximated with the data measured at 44 K, and $I(Q)$ is a scaling factor. Depending on sample composition and temperature, one (n = 1) or two (n = 2) Lorentzians were needed to adequately describe the QENS signal.

Fig. 4 shows $S(Q,E)$ at the lowest and highest measured temperatures, 270 and 375 K, for both materials. Data are shown for Q = 1.6 Å^{-1} and included in the plots are the fits according to eqn (1). Data at all temperatures are shown in Fig. S4 and S5. The $S(Q,E)$ at 270 and 300 K can be adequately fitted to one Lorentzian (L_1), whereas $S(Q,E)$ at $T \geq$ 325 K requires the use of two Lorentzians (L_1 and L_2), for both materials. This indicates significant changes in the dynamics with increasing temperature, especially the observation of at least one more picosecond-timescale dynamical process at the three highest temperatures, but only small (if any) differences in the observed organic cation dynamics between the two materials. Importantly, the FWHM of the two Lorentzians, Γ_1 (narrower) and Γ_2 (broader), does not show any dependency on Q at any of the measured temperatures or for any of the two materials (Fig. 5). Note, the data points for Q < 1 Å^{-1} are considered to be less reliable, because of weaker quasielastic scattering in this range and the possible contribution of small angle scattering due to the powder nature of the samples; therefore, these data points are not considered. The practically Q-independent behavior of the data suggests that the probed dynamics are localized in nature. This is exactly as expected, because of the relatively short timescale of the dynamics as probed here (0.3–13 ps). To increase the robustness of our analysis, we refitted the $S(Q,E)$ with Γ_1 and Γ_2 fixed to their Q-independent mean values (shown as dashed lines in Fig. 5). Notably, the refitting of $S(Q,E)$ did not have any visible effect on the quality of the fits to $S(Q,E)$, which supports our approach.

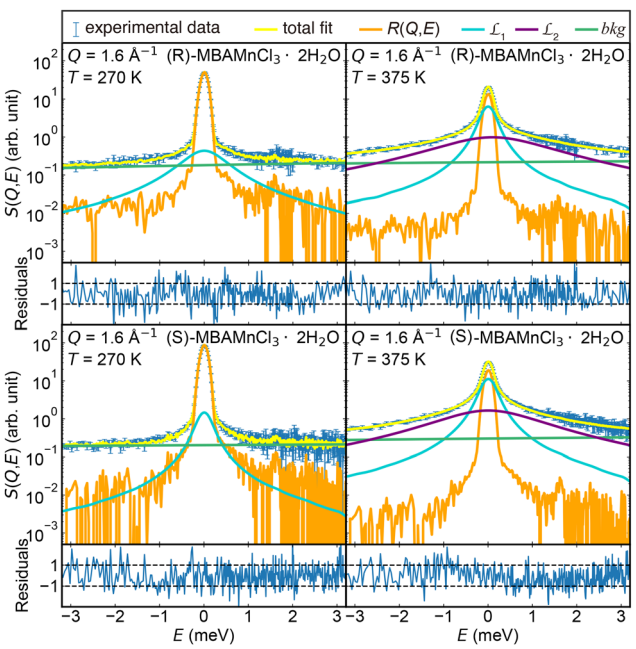

Fig. 4 $S(Q,E)$ of (R)-/(S)-MBAMnCl$_3$·2H$_2$O, together with free fits according to eqn (1), at 270 and 375 K, respectively, and Q = 1.6 Å^{-1}.

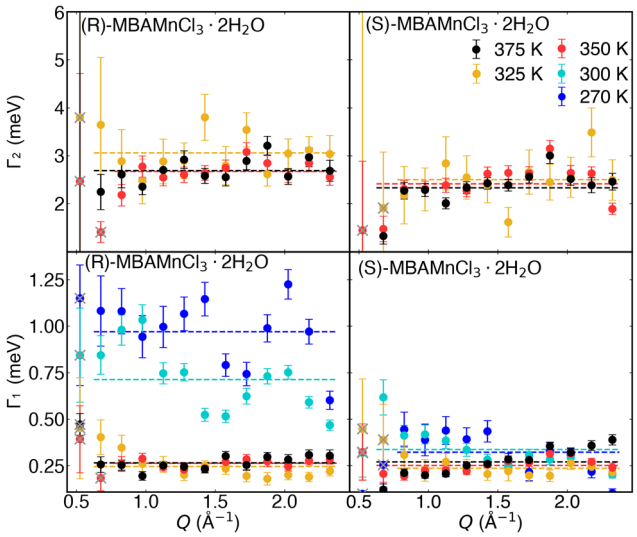

Fig. 5 FWHM of the Lorentzians, Γ_1 and Γ_2, of (R)-/(S)-MBAMnCl$_3$·2H$_2$O, as extracted from the data. Dashed lines are fits to a constant value at each temperature. Data points marked with grey crosses are outliers, not taken into account in the fits.

Fig. 6 shows a plot of the temperature dependence of the correlation time of the dynamics, τ_1 and τ_2, as derived by taking $\tau_i = 2\hbar/\Gamma_i$ (i = 1 and 2).[38] As can be seen, the correlation times of the two dynamics processes are (within error) practically temperature independent between 325 and 375 K and take on values of about 5 ps for the slower process and 0.5 ps for the faster. It follows that there is no strong difference in the correlation time of the observed dynamics between the two materials. The fact that the data show no significant temperature dependence in this temperature range suggests that our measurements are not sensitive enough to capture the correspondingly low activation energy of the dynamics. At the lower temperatures, 270 and 300 K, we find that the correlation time for the slower process is somewhat faster for (R)-MBAMnCl$_3$·2H$_2$O ($\tau_1 \approx$ 2 ps) than for (S)-MBAMnCl$_3$·2H$_2$O ($\tau_1 \approx$ 5 ps). This is in agreement with the

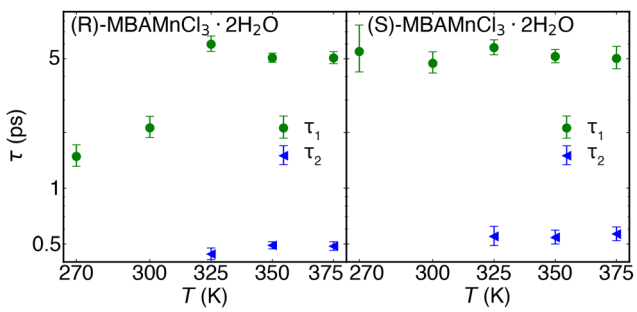

Fig. 6 Temperature dependence of the correlation times, τ_1 and τ_2, for (R)-/(S)-MBAMnCl$_3$·2H$_2$O, as extracted from the data.

observation of the somewhat broader quasielastic scattering at the relatively low-temperature range for (*R*)-MBAMnCl$_3$·2H$_2$O in the $I(T,E)$ maps, as shown in Fig. 3.

3.3 Elastic incoherent structure factor

Information about the spatial geometry of the localized, reorientational dynamics of the organic cations can be obtained from analysis of the elastic incoherent structure factor (EISF), which is defined as the ratio of the elastic and total scattering intensity, *i.e.* $\mathrm{EISF} = A_0(Q)/[A_0(Q) + \sum A_i(Q)]$. Fig. 7 shows the EISFs at 270, 300, 325, 350, and 375 K, as extracted from the data (markers), together with geometrically and physically realistic models (lines) of reorientational dynamics of the H atoms on the MBA cations.

The experimentally determined EISFs exhibit a decreasing trend with increasing Q and temperature, quite similarly for the two different materials. The systematic decrease with increasing temperature suggests an increase in the number of atoms undergoing the dynamics and hence contributing to the QENS signal within the energy range as probed here. At the three lowest temperatures, 270, 300, and 325 K, the EISF can be best approximated with the model for three-fold (C_3) or continuous ($C_{cont.}$) rotational diffusion of the –CH$_3$ and –NH$_3$ groups, together with a constant c, which fit equally well to both materials. The constant c accounts for additional elastic scattering, probably mostly due to H that experiences motions too slow to be resolved by the instrument resolution, which corresponds to dynamics characterized at a timescale of ~0.3–13 ps. c decreases with increasing temperature for both materials. The somewhat larger value of c at 325 K for (*S*)-MBAMnCl$_3$·2H$_2$O (c = 0.18), as compared to (*R*)-MBAMnCl$_3$·2H$_2$O (c = 0), suggests that a larger portion of the –CH$_3$ and –NH$_3$ groups are dynamically immobile in (*S*)-MBAMnCl$_3$·2H$_2$O at this temperature. This is in agreement with the slightly higher onset temperature of the dynamics for (*S*)-MBAMnCl$_3$·2H$_2$O, as shown in Fig. 2 and 3.

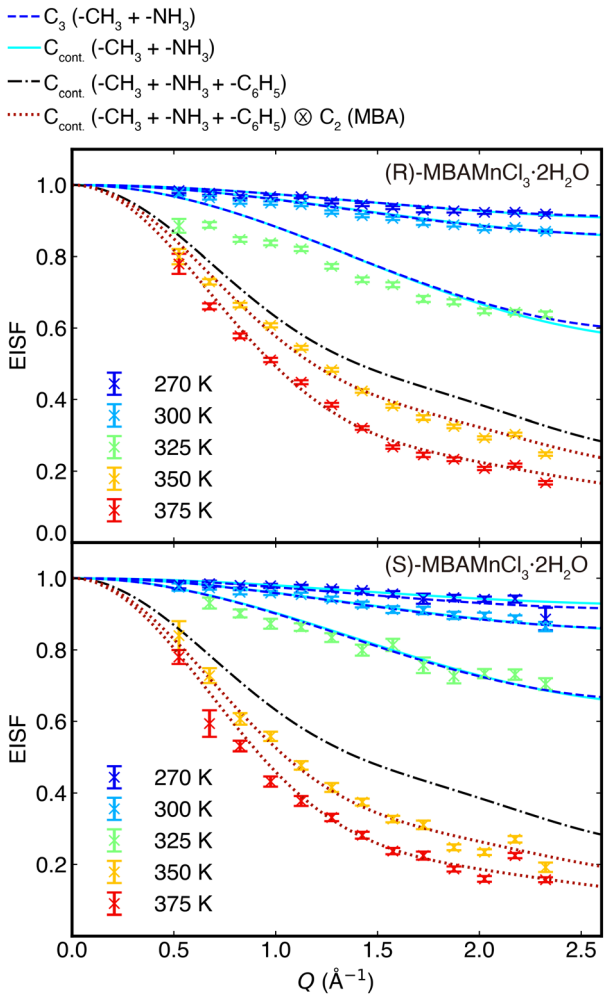

Fig. 7 Experimental EISF (markers) for (a) (*R*)-MBAMnCl$_3$·2H$_2$O and (b) (*S*)-MBAMnCl$_3$·2H$_2$O, together with fits to various jump-diffusion models. The EIFS were extracted from the data.

At even higher temperatures, 350 and 375 K, the EISF shows a more pronounced decrease with increasing Q, which reflects more complex dynamics. This is in agreement with the need for using two Lorentzian functions to fit the QENS spectra. The addition of a dynamical component that takes into account $C_{cont.}$ rotational diffusion of the –C$_6$H$_5$ group leads to a lowering of the EISF, but not enough to fit the experimental data (*cf.* dashed black curve shown in Fig. 7). In this context, we note that the MBA cation may exhibit two possible orientations in the structure. These refer to the cases when the terminal –NH$_3$ group points towards any of the two Cl$^-$ ions of a neighboring $[Mn_2Cl_8(H_2O)_4]^{2-}$ dimer. Effectively, these two cation orientations differ by a rotation of 48° around the molecule's mass center, which means that the change in orientation of the MBA cation may be described as a C_2 jump-diffusion mechanism between the two orientations. Indeed, a model which contains the $C_{cont.}$ rotational diffusion of the –CH$_3$, –NH$_3$, and –C$_6$H$_5$ groups, together with such a C_2 model for a portion of the MBA cations yields an excellent agreement with the experimental data (Fig. 7). A schematic illustration of the dynamics models considered in our analysis is shown in Fig. 8. Mathematical expressions for all models are given in Section S3. A compilation of our tentative assignments of the localized dynamics, as based on our fitting of the EISF data, is shown in Table 1.

4 Discussion

By bringing together the results from the QENS analysis, we can now understand several new features pertaining to the organic cation dynamics in (*R*)-/(*S*)-MBAMnCl$_3$·2H$_2$O.

A general observation is that the localized dynamics of the (*R*)-/(*S*)-MBA cations is highly temperature-dependent, evolving from C_3 or $C_{cont.}$ rotational diffusion of the –CH$_3$ and –NH$_3$ groups at temperatures between 270 and 325 K, to the additional presence of $C_{cont.}$ rotational diffusion of the –C$_6$H$_5$ group and C_2 rotational diffusion of the whole (*R*)-/(*S*)-MBA cation at 350 and 375 K, for both materials.

The observation of room- to lower-temperature dynamics assigned to C_3 or $C_{cont.}$ rotational dynamics of the terminal –CH$_3$ and –NH$_3$ groups have been found in QENS studies of

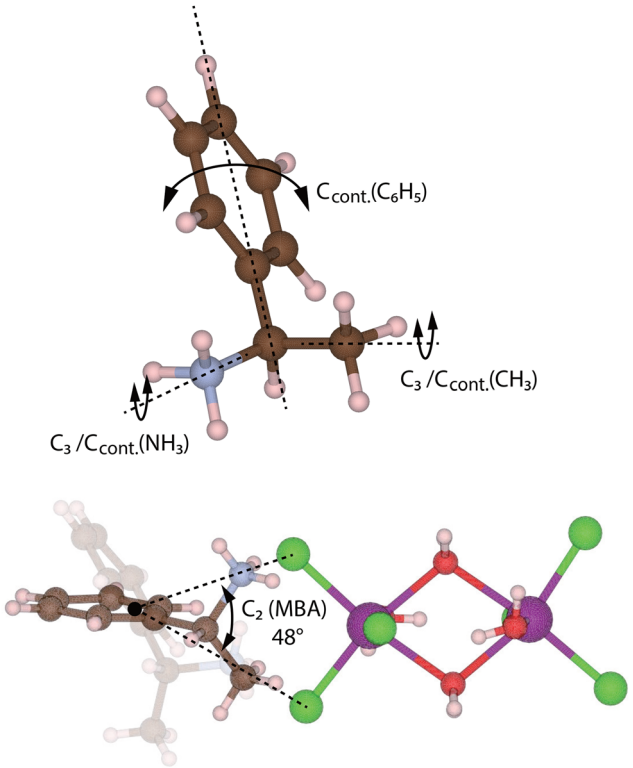

Fig. 8 Schematic illustration of localized dynamics of the (*R*)-MBA cations, as considered in the EISF analysis: (upper) C_3 and $C_{cont.}$ rotational diffusion of the $-CH_3$ and $-NH_3$ groups, $C_{cont.}$ rotational diffusion of the $-C_6H_5$ group, and (lower) C_2 rotational diffusion of the whole MBA cation around its mass center.

Table 1 Compilation of dynamics data obtained from the fitting of the experimental EISFs

Materials	T (K)	c	Tentative assignments of localized dynamics
(*R*)-$MBAMnCl_3{\cdot}2H_2O$	270	0.78	C_3 ($-CH_3$ + $-NH_3$)
	270	0.78	$C_{cont.}$ ($-CH_3$ + $-NH_3$)
	300	0.65	C_3 ($-CH_3$ + $-NH_3$)
	300	0.66	$C_{cont.}$ ($-CH_3$ + $-NH_3$)
	325	0.00	C_3 ($-CH_3$ + $-NH_3$)
	325	0.00	$C_{cont.}$ ($-CH_3$ + $-NH_3$)
	350	0.69[a]	$C_{cont.}$ ($-CH_3$ + $-NH_3$ + $-C_6H_5$) ⊗ C_2 (MBA)
	375	0.21[a]	$C_{cont.}$ ($-CH_3$ + $-NH_3$ + $-C_6H_5$) ⊗ C_2 (MBA)
(*S*)-$MBAMnCl_3{\cdot}2H_2O$	270	0.79	C_3 ($-CH_3$ + $-NH_3$)
	270	0.83	$C_{cont.}$ ($-CH_3$ + $-NH_3$)
	300	0.65	C_3 ($-CH_3$ + $-NH_3$)
	300	0.66	$C_{cont.}$ ($-CH_3$ + $-NH_3$)
	325	0.16	C_3 ($-CH_3$ + $-NH_3$)
	325	0.18	$C_{cont.}$ ($-CH_3$ + $-NH_3$)
	350	0.40[a]	$C_{cont.}$ ($-CH_3$ + $-NH_3$ + $-C_6H_5$) ⊗ C_2 (MBA)
	375	0.02[a]	$C_{cont.}$ ($-CH_3$ + $-NH_3$ + $-C_6H_5$) ⊗ C_2 (MBA)

[a] Refers to the C_2 (MBA) part only.

several other MHPs, including the 3D MHP system $MAPbX_3$ (MA = CH_3NH_3, X = I,[8–11,39,40] Br,[7,12,13,41,42] and Cl[39,43]), and lower-dimensional systems such as $(OA)_2PbI_4$,[19] BA_2PbI_4 and PEA_2PbI_4,[17,18] BA_2PbBr_4, $ODAPbBr_4$ and $GABA_2PbBr_4$,[16] and (1,3-PDA)$PbBr_4$, (1,4-PDA)$PbBr_4$, (1,4-XDA)$PbBr_4$, and (1,3-$XDA)_2PbBr_6$,[20] which thus appears as a generic feature of MHPs containing organic cations with functional $-NH_3$ and/or $-CH_3$ groups, independent of the specific type of organic cation and inorganic sub-lattice. The timescale of the dynamics, however, varies markedly between different materials. As an example, while the timescale of the $-CH_3$ and $-NH_3$ group dynamics in (*R*)-/(*S*)-$MBAMnCl_3{\cdot}2H_2O$ ($\approx$ 0.5–5 ps, T = 270–375 K) is similar to that in 3D MHPs,[9] it is typically faster than for 2D MHPs (usually tens to hundreds of picoseconds).[17,19,44] In this context, we note that the variation in timescale of the dynamics is expected to be primarily affected by the degree of hydrogen/halogen bonding between the $-CH_3/NH_3$ group to the closest halide ion, which is related to the free volume of the solid. A clear example of this is found in the cubic phase of $MAPbX_3$ (X = Cl, Br, and I), for which the timescale of $-CH_3/NH_3$ dynamics decreases systematically with increasing unit cell size.[7,9,39] The generally faster timescale of these dynamics in (*R*)-/(*S*)-$MBAMnCl_3{\cdot}2H_2O$, when compared to 2D MHPs, thus indicates a larger free volume and weaker interactions between the terminal $-CH_3/NH_3$ groups and the inorganic sublattice. This is in agreement with the typically longer hydrogen/halogen-bond distances in layered materials.[7,17,19,44,45] Furthermore, it is probably this relatively large free volume within the 0D framework in (*R*)-/(*S*)-$MBAMnCl_3{\cdot}2H_2O$ that allows for whole-cation reorientation on the relatively short timescale of picoseconds. Whole-cation dynamics have previously only been observed in QENS studies of 3D MHPs with relatively small organic cations, such as for MA and FA dynamics in $(MA,FA)Pb(I,Br,Cl)_3$,[7–14,39–43,46–48] with the exception of one recent report on the high-temperature phase of BA_2PbI_4.[17]

With regard to the comparison of the dynamics data, the lower onset temperature (*cf.* Fig. 3) and generally faster dynamics (*cf.* Fig. 6) of (*R*)-$MBAMnCl_3{\cdot}2H_2O$, when compared to (*S*)-$MBAMnCl_3{\cdot}2H_2O$, may reflect subtle diastereomeric packing effects. Note that these two crystals do not belong to enantiomorphic space groups; thus, strictly speaking, they are not enantiomers. As our XRD data do not reveal any significant differences in their structure, only some minor, statistically insignificant, differences in bond lengths and angles can be observed (see SI). Instead, we speculate that the observed differences may be related to different amounts of hydrogen-containing impurities in the samples, such as ethanol or the new material (*R*)-$MBAMnCl_3{\cdot}C_2H_5OH$ that was found to be present in a small quantity based on our SCXRD and PXRD analyses (see SI).

Finally, we note that the picosecond-timescale dynamics of the (*R*)-/(*S*)-MBA cations induce transient hydrogen/halogen-bonding interactions between the $-CH_3/NH_3$ groups and the inorganic sub-lattice and, in effect, give rise to local structural fluctuations (dynamic disorder) that become increasingly pronounced with increasing temperature. As found for other low-dimensional MHPs,[20] such temperature-dependent dynamic disorder is likely to promote non-radiative recombination of

photoexcited excitons and, hence, to lead to a decrease in the emission intensity upon increasing temperature – an unwanted phenomenon commonly referred to as thermal quenching of luminescence. The relatively high mobility of (*R*)-/(*S*)-MBA cations in (*R*)-/(*S*)-MBAMnCl$_3$·2H$_2$O, due to its unique 0D structure, may thus motivate efforts to tune and restrict the dynamics by structural modification as a route towards higher resistance towards thermal quenching of luminescence.

5 Conclusions

To conclude, our QENS study of (*R*)-/(*S*)-MBAMnCl$_3$·2H$_2$O unravelled the nature of the organic cation, (*R*)-/(*S*)-MBA, dynamics on the picosecond timescale and how it changes with temperature from 44 to 375 K. In the low-temperature regime, up to approximately 270 K, the probed dynamics are limited to (an)harmonic vibrations, whereas at higher temperatures, the (*R*)-/(*S*)-MBA cations undergo reorientational dynamics akin to certain high-symmetry motions. At temperatures between 270 and 325 K, the dynamics data can be described as C_3 or $C_{cont.}$ rotational diffusion of the –CH_3 and –NH_3 groups of the (*R*)-/(*S*)-MBA cation. At higher temperatures, the dynamics data point towards the additional presence of both $C_{cont.}$ rotational diffusion of the –C_6H_5 group of the (*R*)-/(*S*)-MBA cation, as well as C_2 jump-diffusion dynamics of the whole (*R*)-/(*S*)-MBA cation between two different cation orientations. The observation of whole-cation dynamics on the picosecond timescale for large molecules such as (*R*)-/(*S*)-MBA is rare and probably originates from the relatively large free volume with the 0D structure of (*R*)-/(*S*)-MBAMnCl$_3$·2H$_2$O.

Conflicts of interest

There are no conflicts to declare.

Data availability

Data from this article, including the neutron scattering data as measured at the Paul Scherrer Institute (PSI), are available in ref. 49 and 50.

Supplementary information (SI): X-ray diffraction and structural analyses, additional quasielastic neutron scattering data and fits, and additional information about the EISF analysis (PDF). See DOI: https://doi.org/10.1039/d6tc00535g.

CCDC 2379524 and 2379426 contain the supplementary crystallographic data for this paper.[51a,b]

Acknowledgements

This research was funded by the Swedish Research Council (Grant No. 2021-04807 and 2025-04685) and the Swedish Foundation for Strategic Research within the Swedish National Graduate School in Neutron Scattering, SwedNess (Grant No. GSn15-0008). This work is based on experiments performed at the Swiss spallation neutron source SINQ, Paul Scherrer Institute, Villigen, Switzerland.

References

1 A. Kojima, K. Teshima, Y. Shirai and T. Miyasaka, Organometal Halide Perovskites as Visible-Light Sensitizers for Photovoltaic Cells, *J. Am. Chem. Soc.*, 2009, **131**, 6050–6051.
2 N. J. Jeon, J. H. Noh, W. S. Yang, Y. C. Kim, S. Ryo, J. Seo and S. I. Seok, Compositional engineering of perovskite materials for high-performance solar cells, *Nature*, 2015, **517**, 476–480.
3 A. Yangui, D. Garrot, J. S. Lauret, A. Lusson, G. Bouchez, E. Deleporte, S. Pillet, E. E. Bendeif, M. Castro, S. Triki, Y. Abid and K. Boukheddaden, Optical Investigation of Broadband White-Light Emission in Self-Assembled Organic-Inorganic Perovskite $(C_6H_{11}NH_3)_2PbBr_4$, *J. Phys. Chem. C*, 2015, **119**, 23638–23647.
4 M. D. Smith, A. Jaffe, E. R. Dohner, A. M. Lindenberg and H. I. Karunadasa, Structural origins of broadband emission from layered Pb–Br hybrid perovskites, *Chem. Sci.*, 2017, **8**, 4497–4504.
5 J. Y. Kim, J.-W. Lee, H. S. Jung, H. Shin and N.-G. Park, High-Efficiency Perovskite Solar Cells, *Chem. Rev.*, 2020, **120**, 7867–7918.
6 S.-N. Hsu, W. Zhao, Y. Gao, Akriti, M. Segovia, X. Xu, B. W. Boudouris and L. Dou, Thermoelectric performance of lead-free two-dimensional halide perovskites featureing conjugated ligands, *Nano Lett.*, 2021, **21**, 7839–7844.
7 I. P. Swainson, C. Stock, S. F. Parker, L. Van Eijck, M. Russina and J. W. Taylor, From soft harmonic phonons to fast relaxational dynamics in $CH_3NH_3PbBr_3$, *Phys. Rev. B: Condens. Matter Mater. Phys.*, 2015, **92**, 100303(R).
8 A. M. Leguy, J. M. Frost, A. P. McMahon, V. G. Sakai, W. Kockelmann, C. Law, X. Li, F. Foglia, A. Walsh, B. C. O'Regan, J. Nelson, J. T. Cabral and P. R. Barnes, The dynamics of methylammonium ions in hybrid organic-inorganic perovskite solar cells, *Nat. Commun.*, 2015, **6**, 7124.
9 T. Chen, B. J. Foley, B. Ipek, M. Tyagi, J. R. Copley, C. M. Brown, J. J. Choi and S. H. Lee, Rotational dynamics of organic cations in the $CH_3NH_3PbI_3$ perovskite, *Phys. Chem. Chem. Phys.*, 2015, **17**, 31278–31286.
10 B. Li, Y. Kawakita, Y. Liu, M. Wang, M. Matsuura, K. Shibata, S. Ohira-Kawamura, T. Yamada, S. Lin, K. Nakajima and S. F. Liu, Polar rotor scattering as atomic-level origin of low mobility and thermal conductivity of perovskite $CH_3NH_3PbI_3$, *Nat. Commun.*, 2017, **8**, 16086.
11 J. Li, M. Bouchard, P. Reiss, D. Aldakov, S. Pouget, R. Demadrille, C. Aumaitre, B. Frick, D. Djurado, M. Rossi and P. Rinke, Activation Energy of Organic Cation Rotation in $CH_3NH_3PbI_3$ and $CD_3NH_3PbI_3$: Quasi-Elastic Neutron Scattering Measurements and First-Principles Analysis Including Nuclear Quantum Effects, *J. Phys. Chem. Lett.*, 2018, **9**, 3969–3977.

12 V. K. Sharma, R. Mukhopadhyay, A. Mohanty, M. Tyagi, J. P. Embs and D. D. Sarma, Contrasting Behaviors of FA and MA Cations in $APbBr_3$, *J. Phys. Chem. Lett.*, 2020, **11**, 9669–9679.

13 E. M. Mozur, A. E. Maughan, Y. Q. Cheng, A. Hug, N. Jalarvo, L. L. Daemen and J. R. Neilson, Orientational Glass Formation in Substituted Hybrid Perovskites, *Chem. Mater.*, 2017, **29**, 10168–10177.

14 R. Lavén, M. M. Koza, L. Malavasi, A. Perrichon, M. Appel and M. Karlsson, Rotational Dynamics of Organic Cations in Formamidinium Lead Iodide Perovskites, *J. Phys. Chem. Lett.*, 2023, **14**, 2784–2791.

15 N. P. Gallop, O. Selig, G. Giubertoni, H. J. Bakker, Y. L. A. Rezus, J. M. Frost, T. L. C. Jansen, R. Lovrincic and A. A. Bakulin, Rotational Cation Dynamics in Metal Halide Perovskites: Effect on Phonons and Material Properties, *J. Phys. Chem. Lett.*, 2018, **9**, 5987–5997.

16 A. A. Koegel, I. W. H. Oswald, C. Rivera, S. L. Miller, M. J. Fallon, T. R. Prisk, C. M. Brown and J. R. Neilson, Influence of Inorganic Layer Thickness on Methylammonium Dynamics in Hybrid Perovskite Derivatives, *Chem. Mater.*, 2022, **34**, 8316–8323.

17 R. Lavén, M. M. Koza, N. H. Jalarvo, M. Moroni, L. Malavasi and M. Karlsson, Organic Cation Dynamics in the Layered Lead Iodide Perovskites BA_2PbI_4 and PEA_2PbI_4, *J. Phys. Chem. Lett.*, 2025, **16**, 10282–10290.

18 H. S. Rajeev, X. Hu, W.-L. Chen, D. Zhang, T. Chen, M. Kofu, R. Kajimoto, M. Nakamura, A. Z. Chen, G. C. Johnson, M. Yoon, Y.-M. Chang, D. A. Dickie, J. J. Choi and S.-H. Lee, The Influence of Structural Dynamics in Two-Dimensional Hybrid Organic-Inorganic Perovskites on Their Photoluminescence Efficiency - Neutron Scattering Analysis, *J. Phys. Soc. Jpn.*, 2025, **94**, 034602.

19 X. Hu, D. Zhang, T. Chen, A. Z. Chen, E. N. Holmgren, Q. Zhang, D. M. Pajerowski, M. Yoon, G. Xu, J. J. Choi and S. H. Lee, Crystal structures and rotational dynamics of a two-dimensional metal halide perovskite $(OA)_2PbI_4$, *J. Phys. Chem.*, 2020, **152**, 014703.

20 K. Shi, L. Malavasi, F. Juranyi and M. Karlsson, Rotational dynamics of diammonium cations in lead bromide composites investigated by quasi-elastic neutron scattering, *Phys. Chem. Chem. Phys.*, 2026, **28**, 7766–7773.

21 W. D. Cai, J. J. Qin, T. Q. Pang, X. Y. Cai, R. X. Jia and F. Gao, Chirality Induced Crystal Structural Difference in Metal Halide Composites, *Adv. Opt. Mater.*, 2022, **10**, 2102140.

22 W. D. Cai, C. Y. Kuang, T. J. Liu, Y. Q. Shang, J. Zhang, J. J. Qin and F. Gao, Multicolor light emission in manganese-based metal halide composites, *Appl. Phys. Rev.*, 2022, **9**, 041409.

23 S. Wang, Y. Zhang, P. S. Halasyamani and D. B. Mitzi, Chirality and Solvent Coassist the Structural Evolution of Hybrid Manganese Chlorides with Second-Harmonic-Generation Response, *Inorg. Chem.*, 2024, **63**, 16121–16127.

24 J. Ma, H. Wang and D. Li, Recent Progress of Chiral Perovskites: Materials, Synthesis, and Properties, *Adv. Mater.*, 2021, **33**, e2008785.

25 R. F. Service, Lighting the Way to a Quantum Computer, *Science*, 2001, **292**, 2412–2413.

26 O. B. Dor, S. Yochelis, S. P. Mathew, R. Naaman and Y. Paltiel, A chiral-based magnetic memory device without a permanent magnet, *Nat. Commun.*, 2013, **4**, 2256.

27 M. C. Heffern, L. M. Matosziuk and T. J. Meade, Lanthanide Probes for Bioresponsive Imaging, *Chem. Rev.*, 2014, **114**, 4496–4539.

28 D. J. Kissick, D. Wanapun and G. J. Simpson, Second-Order Nonlinear Optical Imaging of Chiral Crystals, *Annu. Rev. Anal. Chem.*, 2011, **4**, 419–437.

29 K. Mishra, D. Guyon, J. San Martin and Y. Yan, Chiral Perovskite Nanocrystals for Asymmetric Reactions: A Highly Enantioselective Strategy for Photocatalytic Synthesis of N–C Axially Chiral Heterocycles, *J. Am. Chem. Soc.*, 2023, **145**, 17242–17252.

30 J. Ahn, E. Lee, J. Tan, W. Yang, B. Kim and J. Moon, A new class of chiral semiconductors: chiral-organic-molecule-incorporating organic-inorganic hybrid perovskites, *Mater. Horiz.*, 2017, **4**, 851–856.

31 J. Mesota, S. Janssen, L. Holitzner and R. Hempelmann, FOCUS: Project of a space and time focussing time-of-flight spectrometer for cold neutrons at the Spallation Source SINQ of the Paul Scherrer Institute, *J. Neutron Res.*, 1996, **3**, 293–310.

32 S. Janssen, J. Mesot, L. Holitzner, A. Furrer and R. Hempelmann, FOCUS: A hybrid TOF-spectrometer at SINQ, *Phys. B*, 1997, **234**, 1174–1176.

33 L. Bian, Proton Donor Is More Important Than Proton Acceptor in Hydrogen Bond Formation: A Universal Equation for Calculation of Hydrogen Bond Strength, *J. Phys. Chem. A*, 2003, **107**, 11517–11524.

34 R. T. Azuah, L. R. Kneller, Y. Qiu, P. L. Tregenna-Piggott, C. M. Brown, J. R. Copley and R. M. Dimeo, DAVE: A Comprehensive Software Suite for the Reduction, Visualization, and Analysis of Low Energy Neutron Spectroscopic Data, *J. Res. Natl. Inst. Stand. Technol.*, 2009, **114**, 341–358.

35 T. Lanigan-Atkins, X. He, M. Krogstad, D. Pajerowski, D. Abernathy, G. N. Xu, Z. Xu, D.-Y. Chung, M. Kantzidis and S. Rosenkranz, *et al.*, Two-dimensional overdamped fluctuations of the soft perovskite lattice in $CsPbBr_3$, *Nat. Mater.*, 2021, **20**, 977–983.

36 Q. Ren, M. K. Gupta, M. Jin, J. Ding, J. Wu, Z. Chen, S. Lin, O. Fabelo, J. A. Rodréguez-Velamazán, M. Kofu, K. Nakajima, M. Wolf, F. Zhu, J. Wang, Z. Cheng, G. Wang, X. Tong, Y. Pei, O. Delaire and J. Ma, Extreme phonon anharmonicity underpins superionic diffusion and ultralow thermal conductivity in argyrodite Ag_8SnSe_6, *Nat. Mater.*, 2023, **22**, 999–1006.

37 R. Lavén, E. Fransson, P. Erhart, F. Juranyi, G. E. Granroth and M. Karlsson, Unraveling the Nature of Vibrational Dynamics in $CsPbI_3$ by Inelastic Neutron Scattering and Molecular Dynamics Simulations, *J. Phys. Chem. Lett.*, 2025, **16**, 4812–4818.

38 M. Bée, *Quasielastic neutron scattering*, Adam Hilger, United Kingdom, 1988.

39 G. Schuck, F. Lehmann, J. Ollivier, H. Mutka and S. Schorr, Influence of Chloride Substitution on the Rotational Dynamics of Methylammonium in $MAPbI_{3-x}Cl_x$ Perovskites, *J. Phys. Chem. C*, 2019, **123**, 11436–11446.

40 V. K. Sharma, R. Mukhopadhyay, A. Mohanty, V. G. Sakai, M. Tyagi and D. D. Sarma, Contrasting Effects of FA Substitution on MA/FA Rotational Dynamics in $FA_xMA_{1-x}PbI_3$, *J. Phys. Chem. C*, 2021, **125**, 13666–13676.

41 K. L. Brown, S. F. Parker, I. R. García, S. Mukhopadhyay, V. García Sakai and C. Stock, Molecular orientational melting within a lead-halide octahedron framework: The order-disorder transition in $CH_3NH_3PbBr_3$, *Phys. Rev. B*, 2017, **96**, 174111.

42 A. Johnston, G. Walters, M. I. Saidaminov, Z. Huang, K. Bertens, N. Jalarvo and E. H. Sargent, Bromine Incorporation and Suppressed Cation Rotation in Mixed-Halide Perovskites, *ACS Nano*, 2020, **14**, 15107–15118.

43 M. Songvilay, Z. Wang, V. G. Sakai, T. Guidi, M. Bari, Z. G. Ye, G. Xu, K. L. Brown, P. M. Gehring and C. Stock, Decoupled molecular and inorganic framework dynamics in $CH_3NH_3PbCl_3$, *Phys. Rev. Mater.*, 2019, **3**, 125406.

44 A. A. Koegel, E. M. Mozur, I. W. H. Oswald, N. H. Jalarvo, T. R. Prisk, M. Tyagi and J. R. Neilson, Correlating Broadband Photoluminescence with Structural Dynamics in Layered Hybrid Halide Perovskites, *J. Am. Chem. Soc.*, 2022, **144**, 1313–1322.

45 T. Chen, B. J. Foley, C. Park, C. M. Brown, L. W. Harriger, J. Lee, J. Ruff, M. Yoon, J. J. Choi and S. H. Lee, Entropy-driven structural transition and kinetic trapping in formamidinium lead iodide perovskite, *Sci. Adv.*, 2016, **2**, e1601650.

46 E. M. Mozur, M. A. Hope, J. C. Trowbridge, D. M. Halat, L. L. Daemen, A. E. Maughan, T. R. Prisk, C. P. Grey and J. R. Neilson, Cesium Substitution Disrupts Concerted Cation Dynamics in Formamidinium Hybrid Perovskites, *Chem. Mater.*, 2020, **32**, 6266–6277.

47 K. Druzbicki, R. Lavén, J. Armstrong, L. Malavasi, F. Fernandez-Alonso and M. Karlsson, Cation Dynamics and Structural Stabilization in Formamidinium Lead Iodide Perovskites, *J. Phys. Chem. Lett.*, 2021, **12**, 3503–3508.

48 V. K. Sharma, R. Mukhopadhyay, A. Mohanty, V. García Sakai, M. Tyagi and D. D. Sarma, Influence of the Halide Ion on the A-Site Dynamics in $FAPbX_3$ (X = Br and Cl), *J. Phys. Chem. C*, 2022, **126**, 7158–7168.

49 M. Karlsson and F. Gao, *Organic cation dynamics in novel two-dimensional lead-free chiral perovskites (PSI)*, 2021.

50 K. Shi and M. Karlsson, *Organic cation dynamics in novel low dimensional lead-free chiral perovskites (PSI)*, 2022.

51 (*a*) CCDC 2379524: Experimental Crystal Structure Determination, 2026, DOI: 10.5517/ccdc.csd.cc2kw2vd; (*b*) CCDC 2379426: Experimental Crystal Structure Determination, 2026, DOI: 10.5517/ccdc.csd.cc2kvzp3.